INORGANIC CHEMISTRY
FRONTIERS

RESEARCH ARTICLE

View Article Online
View Journal | View Issue

Cite this: *Inorg. Chem. Front.*, 2023, **10**, 991

Received 18th October 2022,
Accepted 3rd December 2022

DOI: 10.1039/d2qi02221d

rsc.li/frontiers-inorganic

Orange/cyan emissive sensors of Sb^{3+} for probing water *via* reversible phase transformation in rare-earth-based perovskite crystals†

Yexin Huang,[a] Yuexiao Pan,*[a] Chengdong Peng,[a] Yihong Ding,[a] Hongzhou Lian,[b] Liyi Li*[c] and Jun Lin*[b]

A facile strategy for water probing with visible perception is particularly important for water transport, ecosystem sustainability, and the ocean industry. Here, we have developed a simple technology to probe water content by using the response of the orange/cyan luminescence color of Sb^{3+} emitted from the two novel rare-earth-based perovskite crystals $Rb_2ScCl_5{\cdot}H_2O$ and Rb_3ScCl_6. The reversible transformation between $Rb_2ScCl_5{\cdot}H_2O$ and Rb_3ScCl_6 accompanied by the significant visible perception of the change of the luminescence color can be realized through the dehydration/hydration process in air. In addition to the favorable sensitivity to water, an in-depth study shows that the highly efficient photoluminescence (PL) of Sb^{3+} in both $Rb_2ScCl_5{\cdot}H_2O$ and Rb_3ScCl_6 host matrixes arises from the self-trapped excitons (STEs) rather than the $5s^2$–$5s^15p^1$ transition of Sb^{3+} according to the density functional theory (DFT) calculation. It can be anticipated that this study will provide new insights into the luminescence mechanism of Sb^{3+} in perovskite crystals and a potential application in a sensitive sensor for probing water content.

1 Introduction

A conventional moisture indicator for the validity of a silica gel dryer often relies on the hydration/dehydration process of $CoCl_2$/$[CoCl(H_2O)_5]Cl{\cdot}H_2O$ accompanied by a color change (blue/pink). The reversible switch or transformation in the PL color of luminescence materials responding to water would be an alternative visual sensor for probing water content in the manufacture and transport of chemical industrial products and anti-counterfeiting. The reversible transition between luminescent $CsPbBr_3$ and non-luminescent $CsPb_2Br_5$ has been achieved upon the exposure/removal of water by loading $CsPbBr_3$ NCs into a porous matrix.[1] The emissive light of Sb^{3+} can be sensitively switched between red/yellow in zero-dimensional (0D) halide single crystals $(PPZ)_2SbCl_7{\cdot}5H_2O$ (PPZ = 1-phenylpiperazine) and $Cs_2InBr_5{\cdot}H_2O$:Sb^{3+} ascribed to the insertion/removal of the water molecules into/from the matrixes.[2–4] Environmentally friendly alternatives free of Pb and organics, and possessing high PLQYs and detection sensitivity, are still in demand in the growing field for application in sensors and anti-counterfeiting.

Recently, emerging luminescence materials based on Sb^{3+} doped all-inorganic halide perovskite crystals have become outstanding candidates for promising application in lighting and displays due to their advantages of excellent optical properties including high photoluminescence efficiency and a broad emitting band covering from the visible to near IR region.[5–23] The introduction of Sb^{3+} dopants has led to a significant increase in the intrinsic PL efficiency of the all-inorganic halide perovskite crystals.[7,8] It has been well documented that the Sb^{3+} ion possesses the ns^2 electronic configuration and its excited state is separated into the singlet state $^1P_1$ and triplet state (^3P_n, n = 1, 2, 3). The excitation transitions from the ground $^1S_0$ to singlet state $^1P_1$ are allowed and one of the triplet states $^3P_1$ is partially allowed, whereas the transitions from $^1S_0$ to $^3P_2$ and $^3P_0$ are forbidden.[18–23] However, it is usually hard to make a decision on whether the PL induced by Sb^{3+} doping is attributed to the $5s^2$–$5s^15p^1$ transition of Sb^{3+} or the STEs of the halide perovskite matrix with new trapping states produced by Sb^{3+} because they both are similar in PL spectra, such as broadband emission with a large Stokes shift. It has been reported that the experimental and computational studies reveal that the origin of red PL in $Cs_2InBr_5{\cdot}H_2O$:Sb^{3+} is attributed to STEs induced by a structural deformation,

---

[a] *Key Laboratory of Carbon Materials of Zhejiang Province, College of Chemistry and Materials Engineering, Wenzhou University, Wenzhou 325035, P. R. China. E-mail: yxpan@wzu.edu.cn*
[b] *State Key Laboratory of Rare Earth Resource Utilization, Changchun Institute of Applied Chemistry, Chinese Academy of Sciences, Changchun 130022, P. R. China. E-mail: jlin@ciac.ac.cn*
[c] *Innovative Drug and Imaging Agent R&D Center, Research Institute of Tsinghua, Pearl River Delta, Guangzhou, P. R. China. E-mail: lily@tsinghua-gd.org*

† Electronic supplementary information (ESI) available. See DOI: **https://doi.org/10.1039/d2qi02221d**

whereas the green emission of $Cs_3InCl_6:Sb^{3+}$ NCs is ascribed to the inter-configurational $^3P_1 \rightarrow {}^1S_0$ transition of Sb^{3+}.[4,13] Even though substantial efforts have been devoted to improving the PL efficiency of Sb^{3+}-doped perovskites and the PLQYs are up to 95%, the demand for an in-depth understanding of the luminescence mechanism is booming. Therefore, further evidence should be provided to confirm the underneath mechanism because both the STEs and $^3P_1 \rightarrow {}^1S_0$ transition of Sb^{3+} are actually correlated with the strong Jahn–Teller effect resulting from the introduction of exotic ions. The intense broadband cyan-green and orange-yellow photoluminescence originating from $[SbCl_6]^{3-}$ in $(Rb/Cs)_3InCl_6:Sb^{3+}$ and $[SbCl_5(H_2O)]^{2-}$ in $Cs_2InCl_5{\cdot}H_2O:Sb^{3+}$ has been identified, respectively.[5,6] The corresponding emission colors of $Cs_2InX_5{\cdot}H_2O:Sb^{3+}$ (X = Cl, Br, I) can be expanded into the orange-red region through the compositional substitution of various halides.[4,12] A reversible cyan/yellow emission switch is realized with Sb^{3+} in the transformation of the crystals of A_3InX_6 and $A_2InX_5{\cdot}H_2O$ (A = Cs, Rb; X = Cl, Br) due to the dehydration/hydration process.[5,13,15] Therefore, Sb^{3+} ions in perovskite crystals exhibit distinctly different PL, which can be switched by the addition/removal of H_2O into/from the ligands of the Sb^{3+} octahedron.

Herein, two novel Pb-free perovskite crystals $Rb_2ScCl_5{\cdot}H_2O$ and Rb_3ScCl_6 with rare-earth Sc^{3+} as central ions are identified for the first time, which have similar structures to those of the established $Cs_2ScCl_5{\cdot}H_2O$ and Cs_3ScCl_6 crystals, respectively.[24] The combination of the systematic experimental and computational results validates that the PL spectra of Sb^{3+} in $Rb_2ScCl_5{\cdot}H_2O$ and Rb_3ScCl_6 with PLQYs up to 99% probably originate from STEs rather than the $5s^2$–$5s^15p^1$ transition of Sb^{3+} because the 5p states of Sb^{3+} are far higher than the bottom of the conduction band. The sensitive switch of the orange/cyan luminescence color of Sb^{3+} responding to water is observed, which is ascribed to the reversible transformation between the matrixes of $Rb_2ScCl_5{\cdot}H_2O$ and Rb_3ScCl_6. The results of this work could offer an in-depth understanding of the luminescence mechanism of Sb^{3+} in perovskite crystals and provide new possibilities in water sensors, where both high PLQYs and sensitive water response are strongly desired.

2 Experimental

2.1 Raw materials

For the experiments, the raw material RbCl (99.9%) was purchased from Meryer (Shanghai, China). Sc_2O_3 (99.9%), and Sb_2O_3 (99.9%), hydrochloric acid HCl (36.5 wt%), and ethyl alcohol were purchased from Aladdin (Shanghai, China). All the starting materials for synthesis were purchased commercially and used as received without further purification.

2.2 Synthesis of Sb^{3+} doped $Rb_2ScCl_5{\cdot}H_2O$ single crystals *via* hydrothermal strategy

For the undoped $Rb_2ScCl_5{\cdot}H_2O$ single crystals, 2 mmol of RbCl, 0.5 mmol of Sc_2O_3, and 3 mL of hydrochloric acid were mixed in a 15 mL Teflon liner. The obtained solution was heated in a stainless steel Parr autoclave at 150 °C for 12 h, and then naturally cooled to room temperature. The supernatant solution was removed by tilting the Teflon liner and the precipitated crystals were washed three times with ethyl alcohol and dried at 60 °C for 12 h. The similar experimental procedures were carried out to obtain the Sb^{3+} doped $Rb_2ScCl_5{\cdot}H_2O$ single crystals by replacing x mmol of Sc_2O_3 with Sb_2O_3 (x = 0.0025, 0.005, 0.01, 0.015, 0.025, 0.04, 0.05, 0.075, 0.1) by keeping the stoichiometric ratios.

2.3 A reversible transformation process between Sb^{3+} doped $Rb_2ScCl_5{\cdot}H_2O$ and Rb_3ScCl_6 crystals induced by water

In a typical process, 50 mg of the as-prepared $Rb_2ScCl_5{\cdot}H_2O:Sb^{3+}$ single crystals with orange emission were ground into powder and then heated at different temperatures (100, 150, 200, 220, 230, 240, and 250 °C) for 2 h in an oven. The sintered products with cyan emission were characterized by PL photographs, spectra, and XRD. The dominant component in the final products sintered at 250 °C was confirmed to be $Rb_3ScCl_6:Sb^{3+}$. For the returning transformation procedure, 3 mg of $Rb_3ScCl_6:Sb^{3+}$ powder was separately put in air with/without a glass lid. After 60 min, the $Rb_3ScCl_6:Sb^{3+}$ powder exposed to air changed to be $Rb_2ScCl_5{\cdot}H_2O:Sb^{3+}$ completely while that with an insulating lid maintained the insensible change. The dependence of time required for the transformation procedure on the relative humidity and the contract area was investigated.

2.4 Fabrication and measurement of a WLED with $Rb_2ScCl_5{\cdot}H_2O:Sb^{3+}$

A typical WLED was fabricated using a 360 nm chip, a blue phosphor $BaMgAl_{10}O_{17}:Eu^{2+}$ (BAM:Eu), a green phosphor $BaSrSiO_4:Eu^{2+}$ (BSSO:Eu), and the as-prepared orange phosphor $Rb_2ScCl_5{\cdot}H_2O:Sb^{3+}$. The three phosphors were thoroughly mixed with epoxy resin and coated on the surface of the LED chips. The devices were solidified at 130 °C for 1 h to produce a solid-state WLED.

3 Results and discussion

Single-crystal X-ray diffraction (SCXRD) has been used to determine that the novel single crystal $Rb_2ScCl_5{\cdot}H_2O$ adopts the orthorhombic space group *Pnma* with unit cell parameters of a = 14.003 Å, b = 10.045 Å, c = 7.246 Å, $\alpha = \beta = \gamma$ = 90° (Fig. 1a and Table S1†). The detailed crystal structure parameters of $Rb_2ScCl_5{\cdot}H_2O$ obtained from the single crystal analysis have been compared to those of $Cs_2ScCl_5{\cdot}H_2O$ (Table S2†). In $Rb_2ScCl_5{\cdot}H_2O$ crystals, each rare earth Sc^{3+} ion in a deformed octahedron is coordinated by five Cl^- ions and one H_2O. The bond lengths of Sc–Cl in $Rb_2ScCl_5{\cdot}H_2O$ range from 2.4510(14) to 2.4873(15) Å, which are longer than those from 2.4589(9) to 2.4845(5) Å in $Cs_2ScCl_5{\cdot}H_2O$. Besides, the angle of Cl–Sc–O is 86.591(3)° in $Rb_2ScCl_5{\cdot}H_2O$, which is larger than that of 85.498 (17)° in $Cs_2ScCl_5{\cdot}H_2O$.[24] The results mean the lattice of

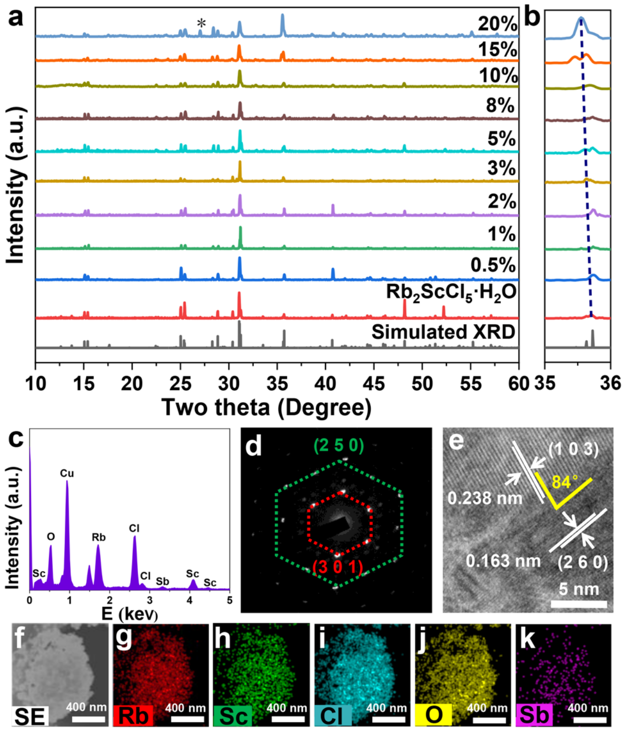

Fig. 1 (a and b) XRD patterns of $Rb_2ScCl_5{\cdot}H_2O{:}x\%Sb^{3+}$ (x = 0, 0.5, 1, 2, 3, 5, 8, 10, 15, and 20) compared to the corresponding simulated result of $Rb_2ScCl_5{\cdot}H_2O$. (c) EDS pattern, (d) SAED, (e) HRTEM, and (f–k) mapping images of the elements in $Rb_2ScCl_5{\cdot}H_2O{:}Sb^{3+}$.

$Rb_2ScCl_5{\cdot}H_2O$ is more easily deformed by doping Sb^{3+} ions and is conducive to producing STEs.[25]

In order to produce PL in $Rb_2ScCl_5{\cdot}H_2O$, parts of Sc^{3+} ions are substituted by equivalent Sb^{3+} ions. The powder X-ray diffraction (PXRD) measurements are carried out to analyze the phase purity after doping Sb^{3+} in different amounts (Fig. 1a). The results show that all the diffraction peaks of the crystals with the doping concentration of Sb^{3+} in 0.5–15 mol% of Sc^{3+} are consistent with simulated orthorhombic $Rb_2ScCl_5{\cdot}H_2O$, indicating the successful introduction of Sb^{3+} ions into the matrix of $Rb_2ScCl_5{\cdot}H_2O$. The sharp diffraction peaks are indicative of the high crystallinity of these crystals doped with various concentrations of Sb^{3+}. Until the doping ratio of Sb^{3+} increases to 20 mol%, an extra diffraction peak can be observed at 27°, which is ascribed to the impurity of the raw material RbCl. With the Sb^{3+} concentration increasing, the XRD diffraction peaks shift to the lower angles (Fig. 1b), demonstrating the expanding of the crystal lattice because the ionic radius of Sb^{3+} (0.92 Å) is larger than that of Sc^{3+} (0.81 Å). Moreover, the EDS pattern of $Rb_2ScCl_5{\cdot}H_2O{:}Sb^{3+}$ with 2 mol% Sb^{3+} dopants confirms the presence of the constituent elements (Rb, Sc, Cl, O, and Sb) without any impurities (Fig. 1c). The selected area electron diffraction (SAED) pattern exhibits two distinct hexagonal diffraction patterns, which correspond to the interplanar distances of the (3 0 1) and (2 5 0) planes of $Rb_2ScCl_5{\cdot}H_2O$ (Fig. 1d). The HRTEM image shows clear lattice spacing of 0.238 and 0.163 nm, which are in good agreement with the (1 0 3) and (2 6 0) planes of the orthorhombic $Rb_2ScCl_5{\cdot}H_2O$ crystal, respectively (Fig. 1e). The elemental mapping images are used to observe the distribution uniformity of each composing element in $Rb_2ScCl_5{\cdot}H_2O{:}Sb^{3+}$ (Fig. 1f–k). It is obvious that the Rb, Sc, Cl, O, and Sb elements are evenly distributed in the whole crystals. XPS measurements were performed to further prove the composition and analyze the chemical states of the elements in the $Rb_2ScCl_5{\cdot}H_2O{:}Sb^{3+}$ crystal (Fig. S1†). The binding energies at 110.98, 109.55, 407.58, 403.05, 199.70, 198.28, 532.18, and 540.31 eV match well with the corresponding spin orbitals of Rb $3d_{3/2}$, Rb $3d_{5/2}$, Sc $2p_{1/2}$, Sc $2p_{3/2}$, Cl $2p_{1/2}$, Cl $2p_{3/2}$, O 1s and Sb 3d, respectively.[26–28]

The PL excitation and emission spectra are illustrated to explore the optical properties of $Rb_2ScCl_5{\cdot}H_2O{:}x\%Sb^{3+}$ (x = 0, 0.5, 1, 2, 3, 5, 8, 10, 15, and 20) crystals (Fig. 2a and b). Pure $Rb_2ScCl_5{\cdot}H_2O$ is non-emissive under ultraviolet (UV) light. For the $Rb_2ScCl_5{\cdot}H_2O{:}xSb^{3+}$ crystals, a single excitation band at 340 nm and a strong broad orange PL emission band at 600 nm with a full width at half maximum (FWHM) of 141 nm have been observed, respectively. As the content of Sb^{3+} increases from 0.5 to 2 mol% of Sb^{3+}, the PL intensity reaches a maximum. The concentration quenching effect occurs after the concentration of Sb^{3+} increases further, which leads to the decrease of the PL intensity. Furthermore, similar PLE spectra manifest that the excited states and dynamics are independent of the content of Sb^{3+}. The dependence of the emission wavelength and intensity of $Rb_2ScCl_5{\cdot}H_2O{:}xSb^{3+}$ on the concentration of Sb^{3+} has been explored (Fig. 2c). A slightly blue shift in the emission spectra of $Rb_2ScCl_5{\cdot}H_2O{:}x\%Sb^{3+}$ can be seen with the increasing concentration of Sb^{3+}. It has been considered that the increase of the Sb^{3+} concentration extends the distance between Sb^{3+} and Cl^- and decreases the magnitude of the crystal field, which brings about a smaller crystal field splitting and a blue shift of the Sb^{3+} emission spectra.[29,30] The full PL excitation spectrum of $Rb_2ScCl_5{\cdot}H_2O{:}Sb^{3+}$ (200–500 nm) monitored at 600 nm shows that there is no additional excitation peak lower than 300 nm (Fig. S2†), which corresponds to the 5p states of Sb^{3+} according to the DFT calculation. It is well documented that for Sb^{3+} with ns^2 excited electronic structure, the ground state is $^1S_0$ and the excited state can be split into four energy states $^1P_1$, $^3P_0$, $^3P_1$, and $^3P_2$. The excitation and emission of Sb^{3+} are usually attributed to the allowed transition between the ground state $^1S_0$ and the excited state $^3P_1$.[31,32] However, the s–p transition of Sb^{3+} and STEs are exactly similar with a broad emission band and a large Stokes shift; thus, more evidence should be provided to elucidate the mechanism responsible for the luminescence of Sb^{3+} in $Rb_2ScCl_5{\cdot}H_2O$ and Rb_3ScCl_6.

The PL lifetimes of $Rb_2ScCl_5{\cdot}H_2O{:}Sb^{3+}$ with different Sb^{3+} concentrations have been measured (Fig. S3†) and all of them can be well-fitted with a singly exponential function. The PL lifetimes decrease monotonously from 1.06 to 0.34 ns with the Sb^{3+} concentrations increasing from 0.5 to 20 mol% (Table S3†), which is due to the increasing energy-transfer probability among the Sb^{3+} ions. The lifetimes of the $Rb_2ScCl_5{\cdot}H_2O$ crystals

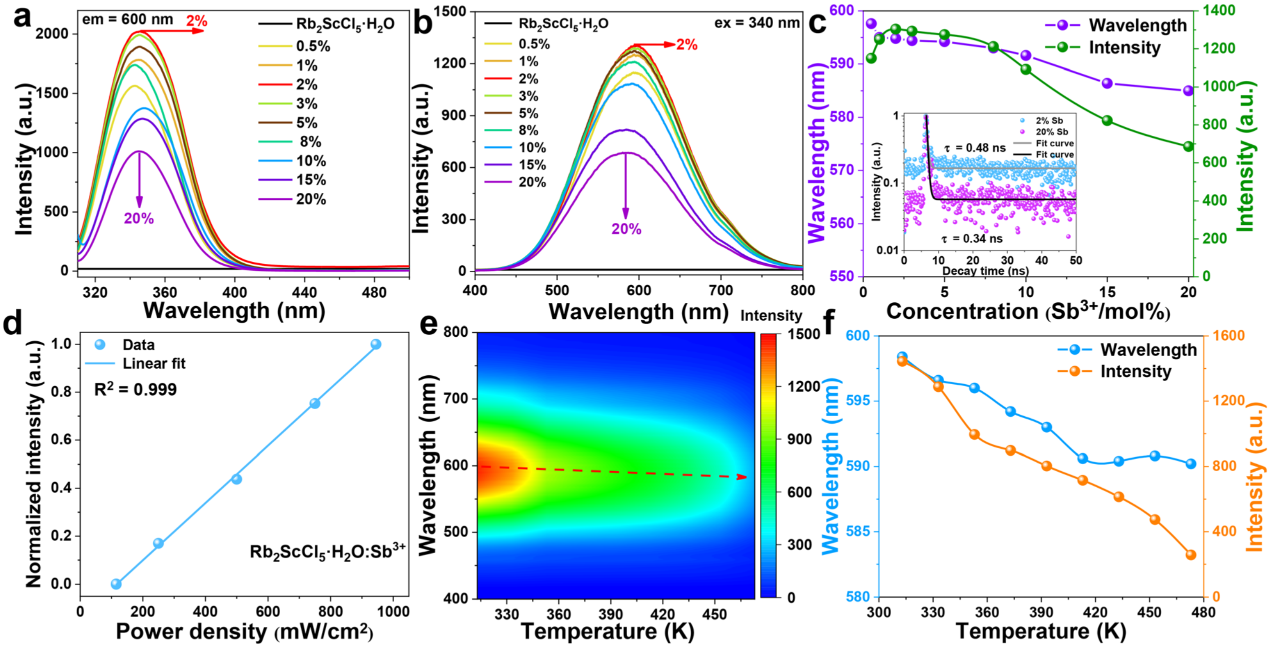

Fig. 2 (a and b) PL excitation (λ_{em} = 600 nm) and emission spectra (λ_{ex} = 340 nm) of $Rb_2ScCl_5{\cdot}H_2O{:}x\%Sb^{3+}$ with different x values. (c) Concentration-dependent emission wavelength and intensity of $Rb_2ScCl_5{\cdot}H_2O{:}xSb^{3+}$ (inset: PL decay curves of $Rb_2ScCl_5{\cdot}H_2O{:}2\%Sb^{3+}$ and $Rb_2ScCl_5{\cdot}H_2O{:}20\%Sb^{3+}$). (d) Linear fitting of the variation of PL intensity with excitation power density and (e) contour map of the temperature-dependent PL emission spectra of $Rb_2ScCl_5{\cdot}H_2O{:}Sb^{3+}$. (f) Emission wavelength and intensity of $Rb_2ScCl_5{\cdot}H_2O{:}Sb^{3+}$ as a function of measurement temperature in the range of 313–473 K.

doped with 2 and 20 mol% Sb^{3+} fitted from the PL decay curves monitored at 600 nm are 0.48 and 0.34 ns, respectively (Inset of Fig. 2c). Such a short decay lifetime is more likely originated from the STE emission owing to the strong Jahn–Teller distortion-induced electron–hole recombination.[33]

To rule out that the emission originated from permanent defects, we have investigated the function of the excitation power on the emission intensity at room temperature. The PL intensity of the emerged emission at 600 nm exhibits a linear dependence on the excitation power density up to 1000 mW cm^{-2}, suggesting that the emission is due to the intrinsic properties of $Rb_2ScCl_5{\cdot}H_2O{:}Sb^{3+}$ rather than permanent defects (Fig. 2d).[34,35] The effect of the high temperature on luminescence can be shown by the contour map and the point-line map (Fig. 2e and f). It can be seen that the PL intensities decrease as the measurement temperature increases from 313 to 473 K, which reflects the intense non-radiative recombination process in the high-temperature region. With the increase in the temperature, the emission band appears to slightly blue-shift from 600 to 585 nm, and this may be attributed to the enhanced electron–phonon coupling at the higher temperature.[8,13,19,24] After a heating–cooling cycle, the PL wavelength returns almost to the initial state and the intensity can reach 80% of the initial strength, indicating the excellent thermal stability of the $Rb_2ScCl_5{\cdot}H_2O{:}Sb^{3+}$ crystals (Fig. S4†). Moreover, the blue-shift has been found in the normalized excitation spectrum and the emission shrinks narrower at 77 K compared to that measured at 298 K (Fig. S5†), which is attributed to the reduction of thermally populated vibrational states at a low temperature.[36,37]

Coordinative H_2O as a part of the Sc^{3+} octahedron is expected to have an important influence on the PL properties of the $Rb_2ScCl_5{\cdot}H_2O{:}Sb^{3+}$ crystals. To investigate the effect of coordinative H_2O, a series of $Rb_2ScCl_5{\cdot}H_2O{:}Sb^{3+}$ crystals have been sintered at different temperatures for 2 h in air. The digital photographs of the $Rb_2ScCl_5{\cdot}H_2O{:}Sb^{3+}$ crystals after heating treatment taken under UV light exhibit the obvious luminescence color changing from orange to white, and finally to cyan when the sintering temperature varies from 100 to 250 °C (Fig. 3a). The sintered crystals are insulated in transparent polyvinyl chloride bags to avoid the re-absorption of water from the atmosphere and characterized by the PL spectra and XRD promptly. The heating-treated $Rb_2ScCl_5{\cdot}H_2O{:}Sb^{3+}$ crystals show a sustained blue shift in the emission peak under 340 nm excitation with the treatment temperature increasing from 100 to 250 °C (Fig. 3b). The samples treated at 220 and 230 °C emit white light compensated by both orange and cyan emissions. The Commission International de L'Elcairage (CIE) coordinates of the samples are experienced from orange to cyan passing the white light region (Fig. S6†). The emission spectrum of the sample sintered at 230 °C can be separated into two bands centered at 590 and 605 nm from the Gaussian fitting PL spectrum (Fig. 3c). Additionally, only the cyan PL is observed in the sample treated at 250 °C.

To elucidate the fundamental reasons responsible for the changing of PL color, the phases of $Rb_2ScCl_5{\cdot}H_2O{:}Sb^{3+}$ crystals

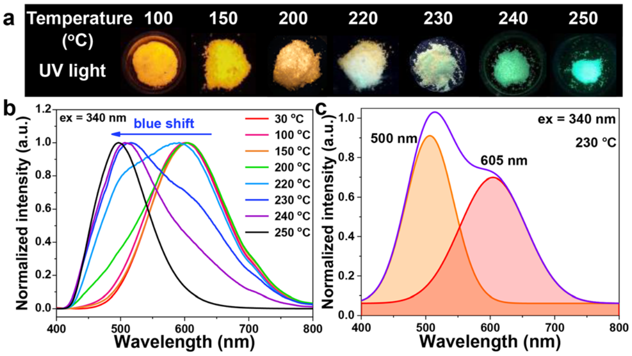

Fig. 3 (a) Digital photographs of $Rb_2ScCl_5{\cdot}H_2O{:}Sb^{3+}$ after treatment at different temperatures taken under 365 nm UV light. (b) Normalized PL emission spectra (λ_{ex} = 340 nm) of $Rb_2ScCl_5{\cdot}H_2O{:}Sb^{3+}$ after treatment at different temperatures. (c) Gaussian fitting PL spectra of $Rb_2ScCl_5{\cdot}H_2O{:}Sb^{3+}$ excited by 340 nm after treatment at 230 °C.

sintered at different temperatures have been characterized by XRD (Fig. 4a). The XRD patterns of the samples treated at a temperature lower than 200 °C can be well indexed to the pure phase of $Rb_2ScCl_5{\cdot}H_2O$ which is almost identical to that of $Rb_2InCl_5{\cdot}H_2O$ in previous work because the ionic radii of In^{3+} and Sc^{3+} are the same as 0.81 Å.[38] The $Rb_2ScCl_5{\cdot}H_2O$ phase is dominantly detected in the samples sintered at a temperature lower than 220 °C. An additional phase is present in those treated at a temperature higher than 230 °C. The dominant phase in the sample after heating $Rb_2ScCl_5{\cdot}H_2O{:}Sb^{3+}$ at 250 °C is supposed to be the Rb_3ScCl_6 phase which is similar to Rb_3InCl_6 (PDF#26-0936). The minor impurity denoted by asterisks is temporarily ascribed to the $RbScCl_4$ phase which is similar to $RbInCl_4$ (PDF#26-0935). Accordingly, the dehydration process at a high temperature is proposed as below:

$$2Rb_2ScCl_5\cdot H_2O : Sb^{3+}(\text{orange}) \rightarrow Rb_3ScCl_6 : Sb^{3+}(\text{cyan}) + RbScCl_4 + 2H_2O$$

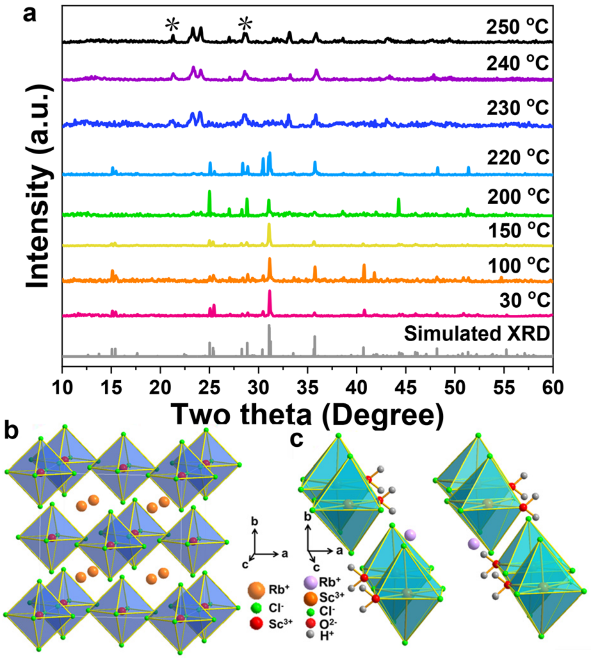

Fig. 4 (a) XRD patterns of $Rb_2ScCl_5{\cdot}H_2O{:}Sb^{3+}$ treated at different temperatures. The asterisks denote the impurity of $RbScCl_4$. Structure projection of (b) Rb_3ScCl_6 and (c) $Rb_2ScCl_5{\cdot}H_2O$ crystals plotted using the software Diamond 3.1.

The regular octahedron $[ScCl_6]^{3-}$ in the Rb_3ScCl_6 crystals is composed of central ions Sc^{3+} coordinated with six same Cl^- ions (Fig. 4b). When the $Rb_3ScCl_6{:}Sb^{3+}$ crystals are exposed to moisture, coordinative H_2O replaces in one of the Cl^- ions and it is transformed into a distorted $[ScCl_5(H_2O)]^{2-}$ octahedron. Consequently, cyan $Rb_3ScCl_6{:}Sb^{3+}$ is transformed into orange $Rb_2ScCl_5{\cdot}H_2O{:}Sb^{3+}$ through the dehydration process at room temperature. In the structure of $Rb_2ScCl_5{\cdot}H_2O$, the individual $[ScCl_5(H_2O)]^{2-}$ octahedra are composed of central ions Sc^{3+} coordinated with five Cl^- ions and one O^{2-} from the H_2O molecule, which breaks the symmetry and subsequently produces a Jahn–Teller distortion (Fig. 4c). It is reasonably speculated that the cyan PL is emitted from $Rb_3ScCl_6{:}Sb^{3+}$ based on the two facts: (i) the crystal $Rb_3InCl_6{:}Sb^{3+}$ emits cyan PL under UV light, and the structure and XRD pattern of Rb_3ScCl_6 are fairly similar to those of Rb_3InCl_6; (ii) no PL is observed in Sb^{3+} doped $RbInCl_4$, and the structures of $RbScCl_4$ and $RbInCl_4$ are identical according to their XRD features.[38] Thus, it is reasonably supposed that the bright cyan PL originated from the $Rb_3ScCl_6{:}Sb^{3+}$ crystals. The TG–DTA curve of $Rb_2ScCl_5{\cdot}H_2O{:}Sb^{3+}$ further demonstrates this transformation process (Fig. S7†). Nearly 7.8% weight loss has been observed up to 250 °C in the TG curve, which corresponds to the loss of coordinative H_2O in $Rb_2ScCl_5{\cdot}H_2O{:}Sb^{3+}$. The weight remains almost constant up to 700 °C, indicating the superior thermal stability of $Rb_3InCl_6{:}Sb^{3+}$.

The PLE spectrum of the $Rb_3ScCl_6{:}Sb^{3+}$ crystals displays a band at 340 nm with a small shoulder at ~325 nm that has similar features to that of the Sb^{3+} doped perovskites (Fig. S8a†).[39,40] The cyan emission spectrum is centered at 500 nm with an FWHM of 100 nm and its decay curve can be fitted to a short-lived PL lifetime of 0.28 ns (98%) and a long-lived PL lifetime of 0.99 ns (2%) by a biexponential function, respectively (Fig. S8b†). Nevertheless, both lifetimes are in the nanosecond scope, which further infers that the recombination routes of Sb^{3+} in the two perovskites are ascribed to the STEs.[33]

A comparison of the optical properties of Sb^{3+} in perovskite crystals formed as $A_2BX_5{\cdot}H_2O$ (A = Cs, Rb; B = In, Sc; and X = Cl, Br) and A_3BX_6 (A = Cs, Rb; B = In, Sc; X = Cl, Br) will give insights into optimizing the PL performance of Sb^{3+} (Table S4†). The undoped crystals $A_2InX_5{\cdot}H_2O$ (A = Rb, Cs; X = Cl, Br) exhibit weak PL with PLQYs lower than 33% and no PL has been observed in the primitive A_3InX_6 (A = Rb, Cs; X = Cl, Br) crystals. Upon doping Sb^{3+}, the $Cs_2InCl_5{\cdot}H_2O{:}Sb^{3+}$ crystals exhibit orange PL with wavelengths located from 560 to 610 nm and PLQYs up to 95%. The PL of $Cs_2InBr_5{\cdot}H_2O{:}Sb^{3+}$

shifts to the deep red region (630–692 nm) compared to that of $Cs_2InCl_5 \cdot H_2O:Sb^{3+}$ due to the expansion of crystal lattices resulted from the substitution of Br^- for Cl^-. A similar redshift of PL from 745 to 823 nm has also been observed from the Sb^{3+} doped Cs_2ZnX_4 matrix with X varying from Cl^- to Br^-.[41] Besides halogens, the alkali cations in A-sites and the centers of the octahedron in B-sites have also significant influences on the PL spectra and PLQYs of the STEs from Sb^{3+}. The A_3InX_6:Sb^{3+} (A = Rb, Cs; X = Cl, Br) crystals show cyan PL with wavelengths located from 497 to 522 nm, and the maximum PLQY of 95% is obtained in $Rb_3InCl_6:Sb^{3+}$. Thus, it is concluded that the PL of Sb^{3+} can be switched by the transformation between $A_2InX_5 \cdot H_2O$ and A_3InX_6 with the removal/addition of H_2O ligands.

The returning process from cyan to orange PL due to the transformation from $Rb_3ScCl_6:Sb^{3+}$ to $Rb_2ScCl_5 \cdot H_2O:Sb^{3+}$ can be realized by the hydration process under an ambient atmosphere. A series of digital photographs with a gradual change in the PL color are illustrated to depict the hydration process of $Rb_3ScCl_6:Sb^{3+}$ stored under an ambient atmosphere and a closed atmosphere (Fig. 5a). After 60 min, the $Rb_3ScCl_6:Sb^{3+}$ crystals exposed to air turn back to orange while those insulated from the air by a transparent glass lid maintain cyan, which definitely demonstrates the hydration process by absorbing H_2O from the air. Therefore, the above results indicate that the octahedral ligands (H_2O or Cl^-) have a great influence on the position of the STE state and the recombination time of STEs.

The gradual change in the PL emission color of Sb^{3+} in Sc-based perovskites has been observed from 600 to 500 nm after dehydration because of the gradual distortion of octahedra (Fig. 5b). Their Commission International de L'Elcairage (CIE) coordinates shift from cyan back to orange on account of the phase transformation from Rb_3ScCl_6 to $Rb_2ScCl_5 \cdot H_2O$ (Fig. S9†). The rates of phase transformation are strongly dependent on the humidity of the environment and the contact areas of the samples exposed to the atmosphere. The times required for transformation are 1 h and 3 s by placing $Rb_3ScCl_6:Sb^{3+}$ under an ambient atmosphere and in concentrated hydrochloric acid, respectively. The resulted products are confirmed further by XRD patterns, which indicate that the dominant phase $Rb_2ScCl_5 \cdot H_2O$ is accompanied by the minor impurity of RbCl (Fig. S10†). Thus, the probable reaction equation for the reversible transformation is shown below:

$$\begin{aligned} &Rb_3ScCl_6 : Sb^{3+}(\text{cyan}) + H_2O \\ &\rightarrow Rb_2ScCl_5 \cdot H_2O : Sb^{3+}(\text{orange}) + RbCl \end{aligned}$$

To further discuss the rate of the transformation, the times taken in the transformation from $Rb_3ScCl_6:Sb^{3+}$ to $Rb_2ScCl_5 \cdot H_2O:Sb^{3+}$ under different contact areas and relative humidity are illustrated (Fig. 5c). As the relative humidity increases from 40% to 80%, the phase transition time decreases gradually from 102 to 29 min. Meanwhile, it shows an increasing time from 34 to 88 min with a decreasing contact area. Therefore, the larger the relative humidity and the bigger the contact area, the shorter the phase transition time required for the transformation from $Rb_3ScCl_6:Sb^{3+}$ to $Rb_2ScCl_5 \cdot H_2O:Sb^{3+}$. Briefly, this merit enables the two novel Sb^{3+} doped Sc-based perovskites to act as potential candidates for a sensitive luminescent sensor for probing humidity.[39]

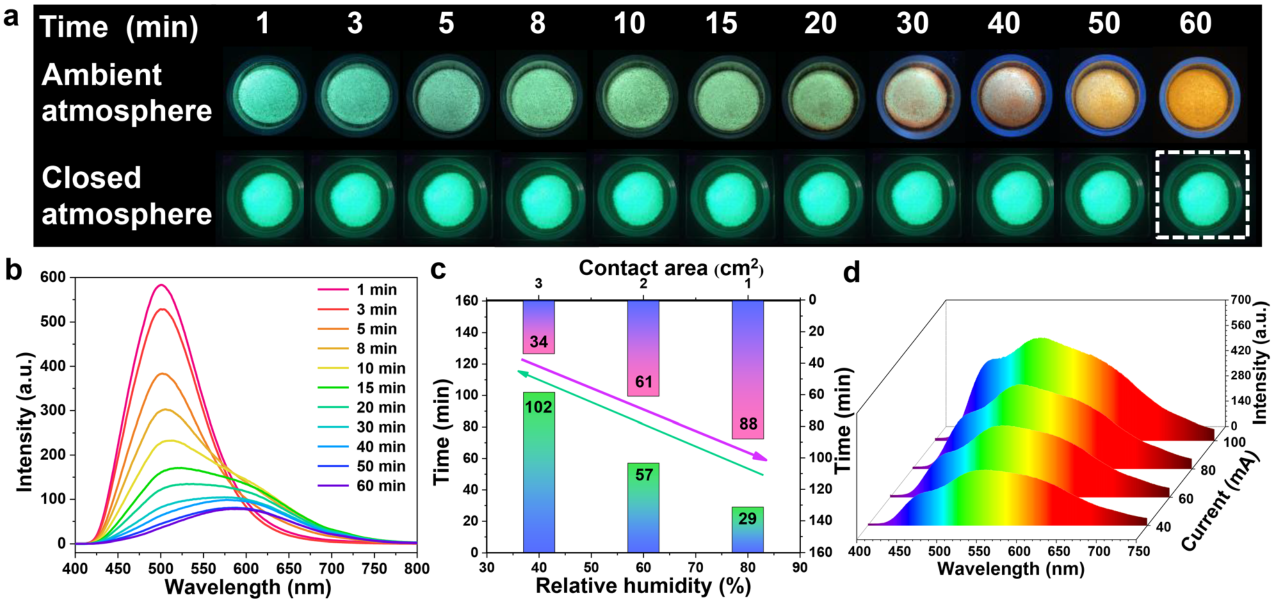

Fig. 5 (a) Digital photographs of the cyan sample (top) exposed in and (bottom) isolated from air under an ambient atmosphere for 60 min. (b) PL emission spectra (λ_{ex} = 340 nm) of $Rb_3ScCl_6:Sb^{3+}$ changing with the aging time. (c) The times consumed in the PL color of Sb^{3+} based on the transformation from Rb_3ScCl_6 to $Rb_2ScCl_5 \cdot H_2O$ dependent on the contact areas (top) and relative humidity (bottom). (d) Waterfall plot of driven current-dependent EL spectra.

A typical WLED is fabricated with the orange phosphor $Rb_2ScCl_5{\cdot}H_2O{:}Sb^{3+}$ combined with the green phosphor $BaSrSiO_4{:}Eu^{2+}$ (BSSO:Eu) and the blue phosphor $BaMgAl_{10}O_{17}{:}Eu^{2+}$ (BAM:Eu) on a 360 nm InGaN chip. As shown in Fig. S11a,† the WLED device exhibits bright electroluminescence (EL) at an operating current of 40 mA, with a color coordinate of (0.3655, 0.3891) and a white-light correlated color temperature (CCT) of 4451 K (Fig. S11b†). Moreover, to confirm the excellent color stability, the EL spectra of the WLED driven under different operating currents are recorded as shown in Fig. 5d, and it is observed that they show similar shapes and positions except for the intensities.

To understand the Sb^{3+}-induced optical properties and PL mechanism, the charge densities, band structure, and partial densities of states (DOS) of the primitive and Sb^{3+} doped Rb_3ScCl_6 and $Rb_2ScCl_5{\cdot}H_2O$ crystals are analyzed by density functional theory (DFT) calculations. The band gaps of the primitive Rb_3ScCl_6 and $Rb_2ScCl_5{\cdot}H_2O$ crystals are calculated to be 3.95 and 3.89 eV (Fig. S12 and S13†), respectively. After doping with Sb^{3+}, the band gaps of the Sb^{3+}-doped Rb_3ScCl_6 and $Rb_2ScCl_5{\cdot}H_2O$ crystals are reduced to 3.18 and 3.11 eV, (Fig. 6), respectively. The results indicate that the introduction of exotic Sb^{3+} ions into a low-dimensional crystal lattice of Rb_3ScCl_6 and $Rb_2ScCl_5{\cdot}H_2O$ would significantly decrease the bandgaps by the formation of Sb-s and Cl-p/O-p orbitals between the valence band (VB) and the conduction band (CB).[8,42] Additionally, the electronic states of the valence band maximum (VBM) of the Sb^{3+}-doped Rb_3ScCl_6 crystals are comprised of the Sb-s and Cl-p orbitals and the VBM of Sb^{3+}-doped $Rb_2ScCl_5{\cdot}H_2O$ comes from the Sb-s, Cl-p, and O-p orbitals from H_2O. No orbital hybridization between Sb 5s (or 5p) orbitals and Cl 3p (or O 2p) orbitals has been observed in the calculated results from DOS, which is quite different from that in $Cs_2ZrCl_6{:}Sb^{3+}$ perovskite crystals.[43]

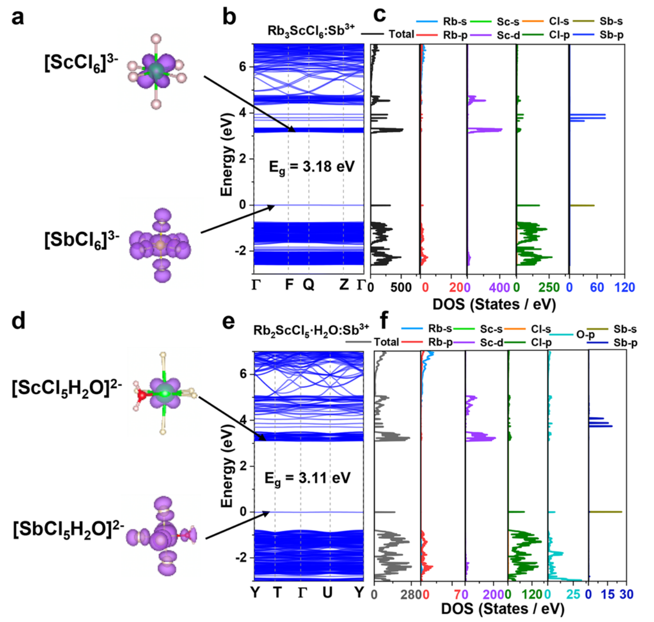

Fig. 6 (a and d) The valence band maximum (VBM) and the conduction band minimum (CBM) associated charge densities of the (a) $[SbCl_6]^{3-}$, $[ScCl_6]^{3-}$ and (d) $[SbCl_5(H_2O)]^{2-}$, $[ScCl_5(H_2O)]^{2-}$centers in $Rb_3ScCl_6{:}Sb^{3+}$ and $Rb_2ScCl_5{\cdot}H_2O{:}Sb^{3+}$ crystals, respectively. (b and e) Calculated electronic band structure and (c and f) density of states of (a–c) $Rb_3ScCl_6{:}Sb^{3+}$ and (d–f) $Rb_2ScCl_5{\cdot}H_2O{:}Sb^{3+}$ crystals.

The conduction band minimum (CBM) states of both the $Rb_3ScCl_6{:}Sb^{3+}$ and $Rb_2ScCl_5{\cdot}H_2O{:}Sb^{3+}$ crystals mainly come from the Sc-d orbitals rather than the Sb-p orbitals (Fig. 6, S14 and S15†). The charges in the CBM are concentrated at the center ions of Sc^{3+} and those in the VBM are distributed uniformly in the whole $[SbCl_6]^{3-}$ octahedron, which signifies that the electrons occupied in the Sb-s orbitals are readily transferred to the Sc-d orbitals upon UV excitation. A higher energy is necessary to promote the Sb-s electrons up to the Sb-p orbitals and non-radiative transition to the Sc-d orbitals would occur subsequently. Thus, these results demonstrate that the dominant contribution for the PL of Sb^{3+}-doped Sc-based perovskite crystals originates from the intrinsic excitons in the host lattice rather than in $[SbCl_6]^{3-}$.[44] The electrons in the ground state are mainly distributed in the $[SbCl_6]^{3-}$ octahedron, while the electrons in the excited state migrate to the $[ScCl_6]^{3-}$ octahedron, which is accompanied by the strong electron–phonon coupling caused by the distortion of the octahedron units after doping.[45] The electrons in the Sb-s orbitals in the ground state can transfer to the Sc-d orbitals by creating trapping energy states upon the excitation of UV light and subsequently transfer back to the ground states. Through non-radiative relaxation and excited-state structural reorganization process, visible light with a large Stokes shift and broadband feature will be produced by the radiative transition process after the recombination of carriers.[43] As presented in the electronic band structure of $Rb_2ScCl_5{\cdot}H_2O{:}Sb^{3+}$ (Fig. 6e and f), the minimum energy for promoting the electrons from the VB to the CB is 3.11 eV (399 nm) and the Sb-p orbitals are located approximately at 4.06 eV (305 nm). There is no excitation band before 320 nm (Fig. S2†), which further indicates that the PL of $Rb_2ScCl_5{\cdot}H_2O{:}Sb^{3+}$ does not originate from the s–p transition of Sb^{3+} but from STEs induced by Jahn–Teller distortion.

Fig. 7 reveals the charge density distributions and local structures of the $[SbCl_6]^{3-}$ octahedron in $Rb_3ScCl_6{:}Sb^{3+}$ and the $[SbCl_5(H_2O)]^{2-}$ octahedron in $Rb_2ScCl_5{\cdot}H_2O{:}Sb^{3+}$. The charge is uniformly distributed around the six Cl^- ions in $[SbCl_6]^{3-}$ because of its symmetrical octahedral structure (Fig. 7a). The introduction of H_2O breaks the symmetrical structure of the octahedron and changes the charge density distribution in the octahedral structure by forming an O–Sb bond in a distorted octahedral structure of $[SbCl_5(H_2O)]^{2-}$. Moreover, most of the charge is observed to be dragged toward H_2O in the $[SbCl_5(H_2O)]^{2-}$ octahedron (Fig. 7b). The local octahedral structures of the $[SbCl_6]^{3-}$ octahedron in $Rb_3ScCl_6{:}Sb^{3+}$ indicate that $[SbCl_6]^{3-}$ possesses the perfect structure, and the Sb–Cl bond length is about 2.65 Å, while the Cl–Sb–Cl angle is 87.6° (Fig. 7c). Meanwhile, the Sb–O bond length reduces to 2.439 Å, and the Cl–Sb–O angle reduces to 87.4° for $[SbCl_5(H_2O)]^{2-}$ in $Rb_2ScCl_5{\cdot}H_2O{:}Sb^{3+}$, which demonstrates the

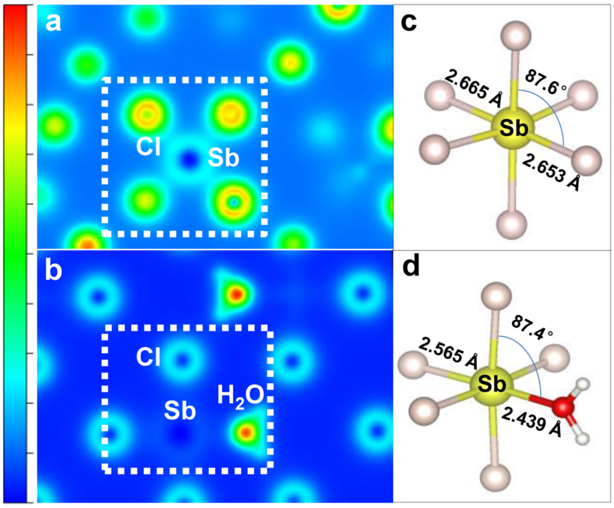

Fig. 7 (a and b) Charge density distribution and (c and d) local structures of (a and c) $[SbCl_6]^{3-}$ in $Rb_3ScCl_6:Sb^{3+}$ and (b and d) $[SbCl_5(H_2O)]^{2-}$ in $Rb_2ScCl_5{\cdot}H_2O:Sb^{3+}$ crystals calculated by DFT.

further evident distortion of the lattice (Fig. 7d). The orbitals between the neighboring Cl-s and Sb-p show few overlaps and the charge carriers from electron transport can be negligible according to the calculated charge density of the best charge density isosurface plane of $[SbCl_6]^{3-}$. Moreover, it is more difficult for the electrons in $[SbCl_5(H_2O)]^{2-}$ to transfer because of the slighter overlap of orbitals from Cl-s, Sb-p, and O-p.

Consequently, combining the theoretical calculation and the experimental characterization results of the optical properties, the luminescence mechanism of $Rb_2ScCl_5{\cdot}H_2O:Sb^{3+}$ and $Rb_3ScCl_6:Sb^{3+}$ is illustrated in Fig. S16.† The electrons in the ground state are promoted to a higher excited state (ES1) and then trapped in $[SbCl_6]^{3-}$ under excitation at 335 nm for $Rb_3ScCl_6:Sb^{3+}$, which subsequently induced the STE1 emission of $Rb_3ScCl_6:Sb^{3+}$ centered at 500 nm. In the same way, upon 340 nm excitation, the low energy will lead to the transfer of electrons to a lower excited state (ES2) and then trapped in $[SbCl_5(H_2O)]^{2-}$ in $Rb_2ScCl_5{\cdot}H_2O:Sb^{3+}$. The electrons follow a self-trapped process to form STE2, and the recombination of electrons from the STE2 state to the ground state yields a wide orange emission at 600 nm with a large Stokes shift.

4 Conclusions

In summary, we have developed a new strategy to probe water content based on the orange/cyan emissive sensors of Sb^{3+} during the reversible phase transformation between the two novel rare-earth-based perovskite crystals $Rb_2ScCl_5{\cdot}H_2O$ and Rb_3ScCl_6 with high PLQYs and sensitivity. The in-depth analysis of the calculated energy of the bottom of the CBM suggests that the luminescence of Sb^{3+} in Sc-based perovskite crystals originates from STEs rather than an s–p transition of Sb^{3+} because the bottom of the CBM mainly consists of the 3d states of Sc^{3+} and the 5p states of Sb^{3+} which are far higher than the bottom of the CBM. After a hydration process through absorbing water in air, the $[ScCl_6]^{3-}$ octahedron is converted into a distorted $[ScCl_5(H_2O)]^{2-}$ octahedron accompanied by the bond length becoming shorter and the charge deviating preferentially toward the H_2O ligand, which causes the emission wavelength of Sb^{3+} to return from the cyan to orange region. This work provides a new water sensor by a switch of the PL color and sheds more light on the importance of the bandgap and charge distribution in determining the luminescence mechanism of Sb^{3+} in low dimensional perovskites.

Conflicts of interest

There are no conflicts to declare.

Acknowledgements

This research is financially supported by the National Natural Science Foundation (NSF) of China (52172152, 51932009, 52172166), the Key Projects of NSF of Zhejiang Province (LZ20E020003, LQ22B010003), the Wenzhou Major Scientific and Technological Innovation Project (ZG2020025), and the Applied Research Programs of Guangdong-Hong Kong-Macao Innovation Center sponsored by Guangzhou Development District.

References

1 X. Y. Yu, L. Z. Wu, D. Yang, M. H. Cao, X. Fan, H. P. Lin, Q. X. Zhong, Y. Xu and Q. Zhang, Hydrochromic $CsPbBr_3$ Nanocrystals for Anti-Counterfeiting, *Angew. Chem., Int. Ed.*, 2020, **59**, 14527–14532.
2 J. B. Luo, J. H. Wei, Z. Z. Zhang and D. B. Kuang, Water-Molecule-Induced Emission Transformation of Zero-Dimension Antimony-Based Metal Halide, *Inorg. Chem.*, 2022, **61**, 338–345.
3 X. L. Li, C. Peng, Y. H. Xiao, D. F. Xue, B. B. Luo and X. C. Huang, Guest-Induced Reversible Phase Transformation of Organic-Inorganic Phenylpiperazinium Antimony(III) Chlorides with Solvatochromic Photoluminescence, *J. Phys. Chem. C*, 2021, **125**, 25112–25118.
4 L. Zhou, J. F. Liao, Z. G. Huang, J. H. Wei, X. D. Wang, W. G. Li, H. Y. Chen, D. B. Kuang and C. Y. Su, A Highly Red-Emissive Lead-Free Indium-Based Perovskite Single Crystal for Sensitive Water Detection, *Angew. Chem., Int. Ed.*, 2019, **58**, 5277–5281.
5 J. D. Majher, M. B. Gray, T. Y. Liu, N. P. Holzapfel and P. M. Woodward, Rb_3InCl_6: A Monoclinic Double Perovskite Derivative with Bright Sb^{3+}-Activated Photoluminescence, *Inorg. Chem.*, 2020, **59**, 14478–14485.
6 P. G. Han, W. Zhou, D. Y. Zheng, X. R. Zhang, C. Li, Q. K. Kong, S. Q. Yan, R. F. Lu and K. L. Han, Lead-Free All

Inorganic Indium Chloride Perovskite Variant Nanocrystals For Efficient Luminescence, *Adv. Opt. Mater.*, 2022, **10**, 2101344.

7 J. C. Jin, Y. H. Peng, Y. T. Xu, K. Han, A. R. Zhang, X. B. Yang and Z. G. Xia, Bright Green Emission from Self-Trapped Excitons Triggered by Sb^{3+} Doping in Rb_4CdCl_6, *Chem. Mater.*, 2022, **34**, 5717–5725.

8 X. F. Meng, Q. L. Wei, W. C. Lin, T. Huang, S. G. Ge, Z. M. Yu and B. S. Zou, Efficient Yellow Self-Trapped Exciton Emission in Sb^{3+}-Doped $RbCdCl_3$ Metal Halides, *Inorg. Chem.*, 2022, **61**, 7143–7152.

9 R. S. Zeng, L. L. Zhang, Y. Xue, B. Ke, Z. Zhao, D. Huang, Q. L. Wei, W. C. Zhou and B. S. Zou, Highly Efficient Blue Emission from Self-Trapped Excitons in Stable Sb^{3+}-Doped $Cs_2NaInCl_6$ Double Perovskites, *J. Phys. Chem. Lett.*, 2020, **11**, 2053–2061.

10 Y. Y. Jing, Y. Liu, M. Z. Li and Z. G. Xia, Photoluminescence of Singlet/Triplet Self-Trapped Excitons in Sb3+-Based Metal Halides, *Adv. Opt. Mater.*, 2021, **9**, 2002213.

11 J. W. Lin, K. J. Liu, H. Ruan, N. Sun, X. Chen, J. Zhao, Z. N. Guo, Q. L. Liu and W. X. Yuan, Zero-Dimensional Lead-Free Halide with Indirect Optical Gap and Enhanced Photoluminescence by Sb Doping, *J. Phys. Chem. Lett.*, 2022, **13**, 198–207.

12 Y. Y. Jing, Y. Liu, X. X. Jiang, M. S. Molokeev, Z. S. Lin and Z. G. Xia, Sb^{3+} Dopant and Halogen Substitution Triggered Highly Efficient and Tunable Emission in Lead-Free Metal Halide Single Crystals, *Chem. Mater.*, 2020, **32**, 5327–5334.

13 Z. L. Gong, W. Zheng, P. Huang, X. W. Cheng, W. Zhang, M. R. Zhang, S. Y. Han and X. Y. Chen, Highly Efficient Sb3+ Emitters in 0D Cesium Indium Chloride Nanocrystals with Switchable Photoluminescence through Water-Triggered Structural Transformation, *Nano Today*, 2022, **44**, 101460.

14 A. Noculak, V. Morad, K. M. McCall, S. Yakunin, Y. Shynkarenko, M. Wörle and M. V. Kovalenko, Bright Blue and Green Luminescence of Sb(III) in Double Perovskite Cs_2MInCl_6 (M = Na, K) Matrices, *Chem. Mater.*, 2020, **32**, 5118–5124.

15 J. L. Huang, T. Chang, R. S. Zeng, J. Yan, Q. L. Wei, W. C. Zhou, S. Cao and B. S. Zou, Controlled Structural Transformation in Sb-Doped Indium Halides A3InCl6 and A2InCl5·H₂O Yields Reversible Green-to-Yellow Emission Switch, *Adv. Opt. Mater.*, 2021, **9**, 2002267.

16 B. Yang and K. L. Han, Ultrafast Dynamics of Self-Trapped Excitons in Lead-Free Perovskite Nanocrystals, *J. Phys. Chem. Lett.*, 2021, **12**, 8256–8262.

17 S. R. Li, J. J. Luo, J. Liu and J. Tang, Self-Trapped Excitons in All-Inorganic Halide Perovskites: Fundamentals, Status, and Potential Applications, *J. Phys. Chem. Lett.*, 2019, **10**, 1999–2007.

18 R. X. Liu, W. J. Zhang, G. J. Li and W. J. Liu, An Ultraviolet Excitation Anti-Counterfeiting Material of Sb^{3+} Doped Cs_2ZrCl_6 Vacancy-Ordered Double Perovskite, *Inorg. Chem. Front.*, 2021, **8**, 4035–4043.

19 H. Arfin and A. Nag, Origin of Luminescence in Sb^{3+}- and Bi^{3+}-Doped Cs_2SnCl_6 Perovskites: Excited State Relaxation and Spin-Orbit Coupling, *J. Phys. Chem. Lett.*, 2021, **12**(41), 10002–10008.

20 C. G. Zhang, M. R. Zhang, W. Zheng, J. J. Wei, S. T. Wang, P. Huang, X. W. Cheng, T. Dao, Z. Chen and X. Y. Chen, A New Class of Luminescent Nanoprobes Based on Main-Group Sb^{3+} emitters, *Nano Res.*, 2022, **15**(1), 179–185.

21 A. S. Kshirsagar, H. Arfin, S. Banerjee, B. Mondal and A. Nag, Colloidal Sb^{3+}-Doped $Cs_2InCl_5{\cdot}H_2O$ Perovskite Nanocrystals with Temperature-Dependent Luminescence, *J. Phys. Chem. C*, 2021, **125**, 27671–27677.

22 X. Y. Liu, X. Xu, B. Li, Y. Q. Liang, Q. Li, H. Jiang and D. S. Xu, Antimony-Doping Induced Highly Efficient Warm-White Emission in Indium-Based Zero-Dimensional Perovskites, *CCS Chem.*, 2020, **2**, 216–224.

23 J. C. Zhou, C. Shi, X. S. Li, Z. M. Sun, Y. J. Ji, J. Deng and B. Wang, A Heterovalent Doping Strategy Induced Efficient Cyan Emission in Sb^{3+}-Doped $CsCdCl_3$ Perovskite Microcrystal for Solid State Lighting, *Ceram. Int.*, 2022, **48**, 28327–28333.

24 R. L. Zhang, X. Xu, X. Mao, Z. Y. Wang, P. Y. Wang, Y. Yang, J. S. Chen, R. F. Lu, W. Q. Deng and K. L. Han, Excitation-Dependent Emission in All-Inorganic Lead-Free Cs2ScCl5·H₂O Perovskite Crystals, *Laser Photonics Rev.*, 2022, 2100689.

25 M. D. Smith and H. I. Karunadasa, White-Light Emission from Layered Halide Perovskites, *Acc. Chem. Res.*, 2018, **51**, 619–627.

26 X. Y. Chen, X. Wang, C. H. An, J. W. Liu and Y. T. Qian, Synthesis of Sb_2O_3 Nanorods under Hydrothermal Conditions, *Mater. Res. Bull.*, 2005, **40**, 469–474.

27 M. F. Hamza, Y. Z. Wei and E. Guibal, Quaternization of Algal/PEI Beads (A New Sorbent): Characterization and Application to Scandium Sorption from Aqueous Solutions, *Chem. Eng. J.*, 2020, **383**, 123210.

28 A. Elizabeth, S. K. Sahoo, H. Phirke, T. Kodalle, T. D. Kühne, J. N. Audinot, T. Wirtz, A. Redinger, C. A. Kaufmann, H. Mirhosseini and H. Mönig, Surface Passivation and Detrimental Heat-Induced Diffusion Effects in RbF-Treated $Cu(In,Ga)Se_2$ Solar Cell Absorbers, *ACS Appl. Mater. Interfaces*, 2022, **14**(29), 34101–34112.

29 J. Y. Zhong, W. D. Zhuang, X. R. Xing, L. G. Wang, Y. F. Li, Y. L. Zheng, R. H. Liu, Y. H. Liu and Y. S. Hu, Blue Shift of Spectrum and Enhanced Luminescent Properties of YAG: Ce^{3+} Phosphor Induced by Small Amount of La^{3+} Incorporation, *J. Alloys Compd.*, 2016, **674**, 93–97.

30 C. J. Liu, X. M. Zhu and Z. F. Zhou, Effects of Composition Modulation on The Structural and Luminescence Properties of Mn^{2+} Doped $Na_2Mg_{1-x}Ca_xSiO_4$ Green-Emitting Phosphors, *Optik*, 2019, **179**, 875–882.

31 M. Z. Liu, C. K. Duan, P. A. Tanner, C. G. Ma and M. Yin, Rationalizing the Photoluminescence of Bi^{3+} and Sb^{3+} in Double Perovskite Halide Crystals, *J. Phys. Chem. C*, 2021, **125**, 26670–26678.

32 Y. Y. Jing, Y. Liu, J. Zhao and Z. G. Xia, Sb^{3+} Doping-Induced Triplet Self-Trapped Excitons Emission in Lead-Free Cs_2SnCl_6 Nanocrystals, *J. Phys. Chem. Lett.*, 2019, **10**, 7439–7444.

33 S. L. Jin, R. F. Li, H. Huang, N. Z. Jiang, J. D. Lin, S. X. Wang, Y. H. Zheng, X. Y. Chen and D. Q. Chen, Compact Ultrabroadband Light-Emitting Diodes Based on Lanthanide-Doped Lead-Free Double Perovskites, *Light: Sci. Appl.*, 2022, **11**, 52.

34 C. Y. Peng, Q. L. Wei, S. F. Yao, X. F. Meng, Z. M. Yu, H. Peng, X. C. Zhong and B. S. Zou, H_2O-NH_4^+-Induced Emission Modulation in Sb^{3+}-Doped $(NH_4)_2InCl_5{\cdot}H_2O$, *Inorg. Chem.*, 2022, **61**, 12406–12414.

35 J. H. Wei, J. B. Luo, J. F. Liao, W. T. Ou and D. B. Kuang, Te^{4+}-Doped $Cs_2InCl_5{\cdot}H_2O$ Single Crystals for Remote Optical Thermometry, *Sci. China Mater.*, 2022, **65**(3), 764–772.

36 J. H. Han, T. Samanta, Y. M. Park, H. B. Cho, J. W. Min, S. J. Hwang, S. W. Jang and W. B. Im, Effect of Self-Trapped Excitons in The Optical Properties of Manganese-Alloyed Hexagonal-Phased Metal Halide Perovskite, *Chem. Eng. J.*, 2022, **450**, 138325.

37 C. K. Zhou, H. R. Lin, Y. Tian, Z. Yuan, R. Clark, B. H. Chen, L. J. Burgt, J. C. Wang, Y. Zhou, K. Hanson, Q. J. Meisner, J. Neu, T. Besara, T. Siegrist, E. Lambers, P. Djurovich and B. W. Ma, Luminescent Zero-Dimensional Organic Metal Halide Hybrids with Near-Unity Quantum Efficiency, *Chem. Sci.*, 2018, **9**, 586–593.

38 P. G. Han, C. Luo, S. Q. Yang, Y. Yang, W. Q. Deng and K. L. Han, All-Inorganic Lead-Free 0D Perovskites by a Doping Strategy to Achieve a PLQY Boost from <2% to 90%, *Angew. Chem., Int. Ed.*, 2020, **59**, 12709–12713.

39 X. W. Cheng, R. F. Li, W. Zheng, D. T. Tu, X. Y. Shang, Z. L. Gong, J. Xu, S. Y. Han and X. Y. Chen, Tailoring the Broadband Emission in All-Inorganic Lead-Free 0D In-Based Halides through Sb3+ Doping, *Adv. Opt. Mater.*, 2021, 2100434.

40 J. Zhou, X. Y. Yun, R. Y. Wang, D. H. Xu and X. Li, Self-Trapped Exciton to Dopant Energy Transfer in Sb3+-Doped Cs2ZrCl6 Perovskite Variants, *Mater. Chem. Front.*, 2021, **5**, 6133.

41 B. B. Su, M. Z. Li, E. H. Song and Z. G. Xia, Sb3+-Doping in Cesium Zinc Halides Single Crystals Enabling High-Efficiency Near-Infrared Emission, *Adv. Funct. Mater.*, 2021, **31**, 2105316.

42 Q. L. Wei, X. F. Meng, W. C. Lin, S. G. Ge, X. X. Han, L. Chen, R. S. Zeng and B. S. Zou, Green Triplet Self-Trapped Exciton Emission in Layered $Rb_3Cd_2Cl_7$:Sb^{3+} Perovskite: Comparison with $RbCdCl_3$:Sb^{3+}, *J. Phys. Chem. Lett.*, 2022, **13**, 8436–8446.

43 B. Chen, Y. Guo, Y. Wang, Z. Liu, Q. Wei, S. X. Wang, A. L. Rogach, G. C. Xing, P. Shi and F. Wang, *J. Am. Chem. Soc.*, 2021, **143**, 17599–17606.

44 Y. R. Dai, Q. L. Wei, T. Chang, J. L. Zhao, S. Cao, B. S. Zou and R. S. Zeng, Efficient Self-Trapped Exciton Emission in Ruddlesden-Popper Sb-Doped $Cs_3Cd_2Cl_7$ Perovskites, *J. Phys. Chem. C*, 2022, **126**, 11238–11245.

45 B. Zhou, Z. X. Liu, S. F. Fang, H. Z. Zhong, B. B. Tian, Y. Wang, H. N. Li, H. L. Hu and Y. M. Shi, Efficient White Photoluminescence from Self-Trapped Excitons in Sb3+/Bi3+-Codoped Cs2NaInCl6 Double Perovskites with Tunable Dual-Emission, *ACS Energy Lett.*, 2021, **6**, 3343–3351.